Basement Structure and Properties of the Western Junggar Basin, China

Junmeng Zhao [ID] *[1, 2, 3], **Shuze Chen**[2, 3], **Gong Deng**[2, 3], **Xuezhong Shao**[4], **Heng Zhang**[2],
Jamshed Aminov[2, 3], **Xinfa Chen**[5], **Zongjin Ma**[3]

1. *Chinese Academy of Sciences (CAS) Center for Excellence in Tibetan Plateau Earth Sciences, Beijing 100101, China*
2. *Key Laboratory of Continental Collision and Plateau Uplift, Institute of Tibetan Plateau Research,*
   Chinese Academy of Sciences, Beijing 100085, China
3. *University of Chinese Academy of Sciences, Beijing 100029, China*
4. *Institute of Geology, China Earthquake Administration, Beijing 100029, China*
5. *Xinjiang Oilfield Company, Karamay 834000, China*

[ID] Junmeng Zhao: https://orcid.org/0000-0003-1389-9425

ABSTRACT: A comprehensive geophysical profile stretching from Qingyijing at the southern edge of the Junggar Basin to Ubara on the northern margin of the Junggar Basin was conducted in an attempt to probe the crustal structure of the western Junggar Basin (hereafter referred to simply as 'the Basin'), and, in particular, the structure and property of the Basin's crystalline basement. A survey using seismically converted waves was conducted along this profile to determine the characteristics of the P- and S-wave velocities typical of the crust and uppermost mantle. A joint inversion of gravitation and aeromagnetic data was also performed to acquire the density and magnetization intensity values found beneath the western Basin. This research revealed that the Basin is composed of the so-called Manasi terrain in the south, and the Wulungu terrain in the north. Their boundary is located along the WNW-trending Dishuiquan-Sangequan suture, linking the NE-striking Da'erbute suture (DS) in the west, and the WNW-trending Kalameili suture (KS) in the east. In its northern part, the Wulungu-type terrain has a double-layered basement, of which the upper layer is a folded basement of Hercynian orogenic origin, and the lower layer is a crystalline basement of Middle–Upper Proterozoic age. The southern part of the Basin, i.e., the Manasi terrain, has a single-layered crystalline basement. The folded basement here is too thin to be clearly distinguished.

KEY WORDS: Junggar Basin, seismically-converted wave, joint inversion of gravity and geomagnetism, basement structure.

0 INTRODUCTION

The Junggar Basin is a typical super-composed basin with a rather complicated structure. The tectonic nature of today's basin is the product of its long-term development and evolution, the study of this evolution has provided the main impetus for oil and gas prospecting and exploration (Wang G et al., 2018; Yang et al., 2017; Zhao et al., 2008a; Zheng et al., 2007, 2000; Wang F Z et al., 2002). Research into the Basin's tectonic structure has dealt principally with two questions: the nature of the structure of its basement (i.e., whether it is single- or double-layered), and the geophysical nature of the basement (i.e., whether it is composed of either continental or oceanic crust).

Zhao (1992) thought that the basement structure could be divided into an upper and a lower layer composed of Paleozoic and Precambrian crystalline blocks, respectively. Kuang (1993) proposed that the Basin's basement was comprised of two conjoined terrains: the Manasi terrain located in the south and composed of old metacrystalline rock; and a young basement called the Wulungu terrain located in the north and including some rigid features, with some sedimentary and metamorphic rocks dating from the Early Cambrian. The Sangequan arc marks the orogenic belt where these two terrains have collided.

One school of thought led by Huang (1979) believed the basement to be composed of continental crust of a Precambrian crystalline nature. Zhang et al. (1991) argued that the Junggar Block was an older block which had existed since at least the Early Precambrian: it, with other nearby blocks, formed the so-called 'Xinjiang Old Land'. Peng (1994) supported Huang's model (Huang, 1979) on the basis of the discovery, in the eastern Basin, of carbonate rocks and granitic gneiss from a typical ~1 900 Ma shallow water continental shelf environment. Yang (1992) proposed that multiple split centers existed in the Junggar-Turpan Basin in the Late Cambrian, between which there were shallows or islands within the larger Neo-Tethyan Ocean. The Basin would therefore have been a back-arc basin of

the Junggar-Turpan Basin during D–P$_1$, with its basement composed of oceanic crust or a newly-grown, folded basement.

There is as yet no common agreement about the structure and nature of the basement of the Basin. This is principally because we do not clearly understand the Basin's deep-seated structure and tectonics. Even though many geophysical explorations have recently been conducted in the Basin, most of these have been aimed at identifying the likely whereabouts of oil and gas. To understand the relation between the Basin's shallow and deep structures and the geodynamic process thereof, it is therefore of vital importance that a detailed picture of the structure of the crust and upper mantle of the Basin and its adjacent regions be reconstructed using comprehensive geophysical methods.

Taking into consideration of the actual working conditions in the studied region, and all that such work entails, we constructed a comprehensive geophysical profile from Qingyijing to Ubara in the western part of the Basin (Fig. 1). Seismic, gravitational and aeromagnetic data were collected and used to acquire a detailed picture of the patterns inherent in the velocity, density and magnetization intensity records of the crust and uppermost mantle along the profile. Finally, by combining our geophysical evidence with geological and geochemical analyses, we reconstructed a possible geodynamic model of the Basin.

1   GEOLOGICAL SETTINGS

The Basin is located on the central Kazakhstan-Junggar Plate (KJP). The KJP exhibits a WNW to E-W strike, and is situated between the Siberian and Tarim plates; its northern and southern boundaries are the Erqisi-Burjing suture (EBS) and the Murzte-Hongliuhe suture (MHS), respectively (Fig. 2).

The KJP reached more or less its present form by the Early Paleozoic, forming a first-order tectonic unit in the area during the Devonian and Carboniferous periods. A second-order tectonic unit was formed at the same time, or later (Fig. 2). These tectonic units, although geographically proximate, have different crustal structures and rock properties, and any interplay between the two would have allowed the formation of new, combined structures. It is clear, therefore, that regional composition and superimposition occurred along the Altay, the Kalameili and the Bogda tectonic belts (N-S trending belts with a transparent northeasterly penetrative structure), forming a series of complicated joint and recombination relations. The Wulungu depression appears to have been produced by a series of compound formations resulting from interplay with the east-west strike Kalameili tectonic belt, the north-west strike Altay-Qinggelidi tectonic belt strike, and the north-south strike tectonic belt of the central Basin. The Manasi-eastern Junggar Basin was produced by a compound interplay between the Kalameili tectonic belt, the Bogda tectonic belt and the Changji-eastern Junggar tectonic system. These tectonic belts were themselves crossed by other tectonic belts in north-south, northwesterly and northeasterly directions.

Because the Basin is largely covered by Meso–Cenozoic sediment, and in addition, tectonic layers lower than the region's Devonian–Carboniferous strata are seldom exposed to the surface in the mountains surrounding it, doubt remains about the structure and properties of the Basin's basement. However, based on comprehensive analyses of geological and geophysical data (Yan et al., 2015; Chen et al., 2014), especially the sedimentary and erosion records of the second-order tectonic units, most scientists
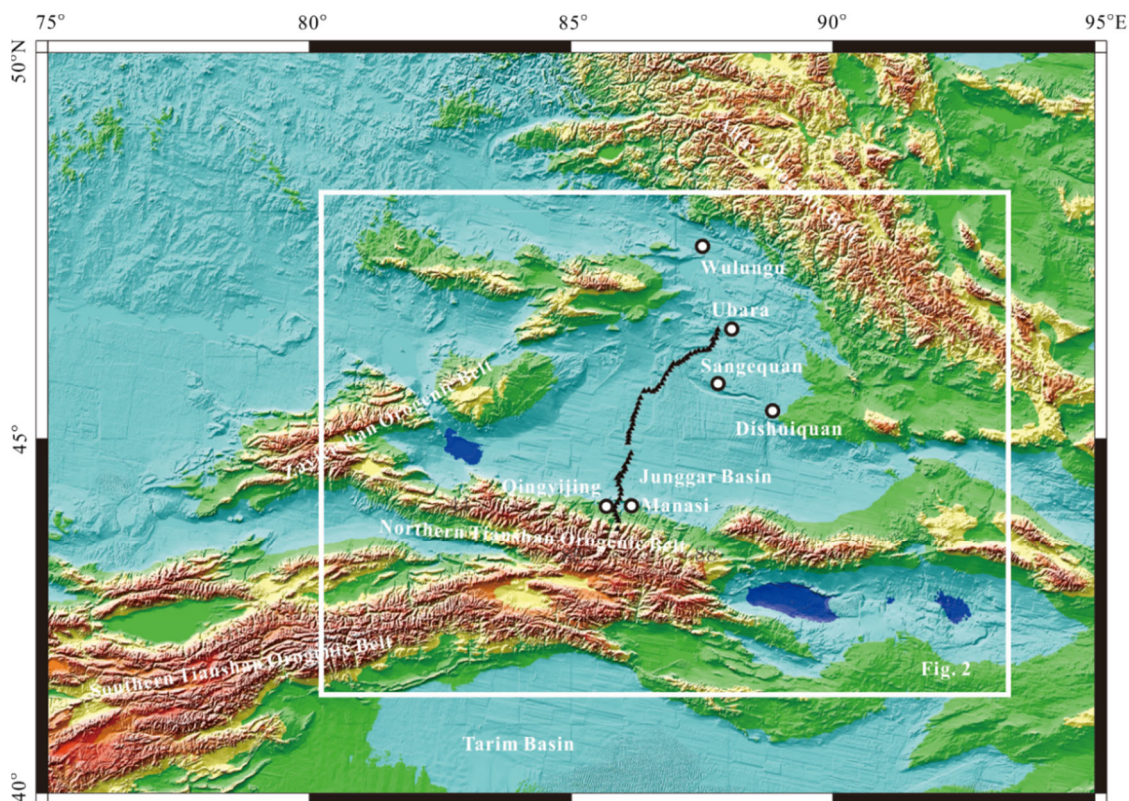

Figure 1. Satellite map showing the location of the profile from Qingyijing to Ubara.
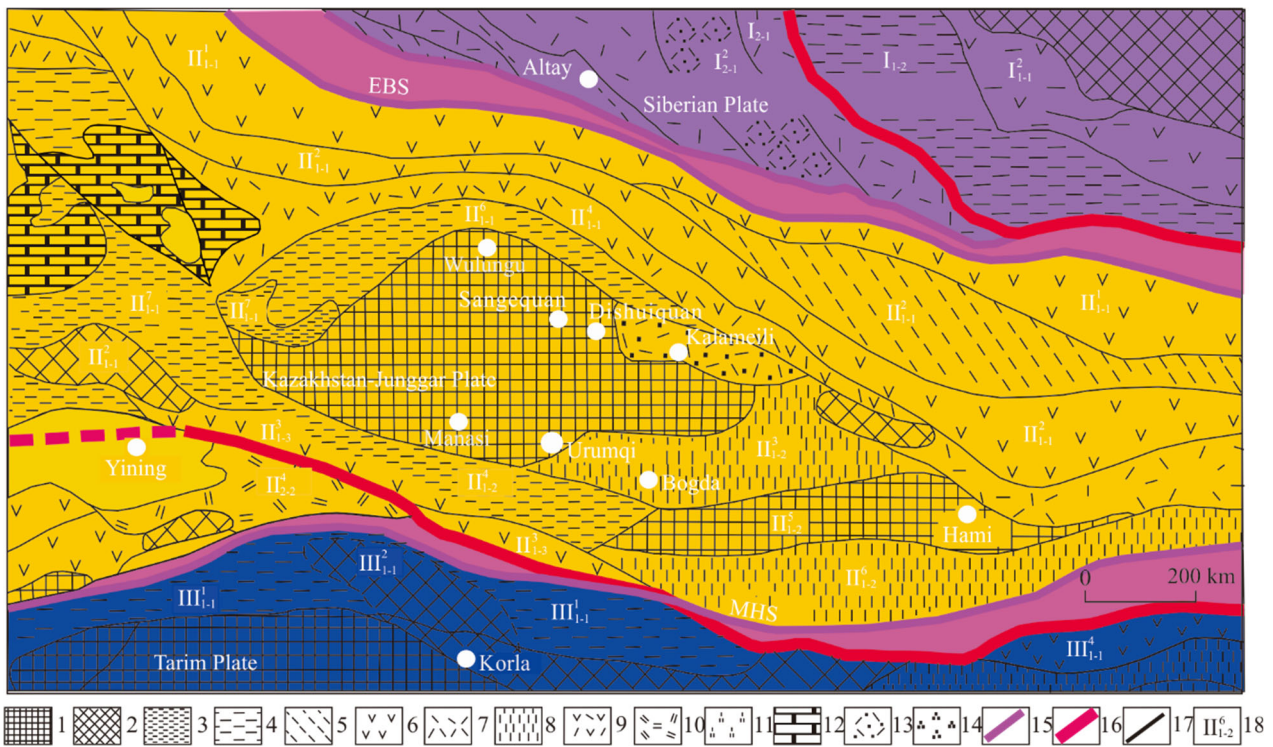
Figure 2. Geological background of the research region. 1. Block with a Mesozoic–Cenozoic covering; 2. block with a Paleozoic covering; 3. residual oceanic basin with exposed Pz1 ophiolites; 4. D–C residual oceanic basin or marginal sea; 5. forearc/back arc basin; 6. island arc; 7. magmatic arc; 8. taphrogenic trough; 9. marginal volcanic rock belt; 10. rift; 11. mélange; 12. area with a Quaternary covering; 13. superposed volcanic sedimentary basin; 14. terrestrial basin; 15. plate suture; 16. microplate boundary; 17. suborder tectonic unit boundary; 18. the number of tectonic units (after Zhao et al., 2003).

now agree that the Basin's basement has not been an integrated block since the Hercynian. Indeed, the eastern Junggar and Wulungu basins exhibit different sedimentary histories. The Wulungu region came into geophysical contact with the Basin in the Late Permian–Early Triassic, while the Manasi region and eastern Junggar Basin did the same as late as the Cenozoic. We were therefore concerned to explore not only the tectonic differences between the Basin and its surrounding mountains, but also the differences among the region's second-order tectonic units.

2   DATA AND METHODS

2.1   Seismic, Gravitational and Aeromagnetic Data

The profile from Qingyijing to Ubara is ~350 km long. Sixty-six seismic stations were installed along the profile (Fig. 1). The mean spacing between these stations was ~5 km, and the recording period was six months. The seismic sensor had a frequency range of 0.5–70 Hz, and the recorder one of 0.7–16 Hz. The band-pass filtering range of the P-wave was 0.5–2 Hz. Different boundaries generate different converted waves, which means boundaries within a layered crust can be recognized by identifying converted phases. Teleseismic events with magnitudes ranging from 4.2 to 7.0 were selected from each station. If the magnitude of any event was <4.2, the energy would be too weak to be recorded by a seismic sensor with such limited sensitivity; at the other end of the scale, the waveform would be too complicated to simulate the converted wave if the magnitude of any event were >7.0. Additionally, all selected events contained strong direct P-wave phases, these being three times larger than secondary reflection waves or other multiples. If we had not done

this, the converted waves produced by secondary reflection waves or other multiples waves would not have been able to be clearly identified. Take account of the above considerations, a total of 55 teleseismic events were studied (Fig. 3).
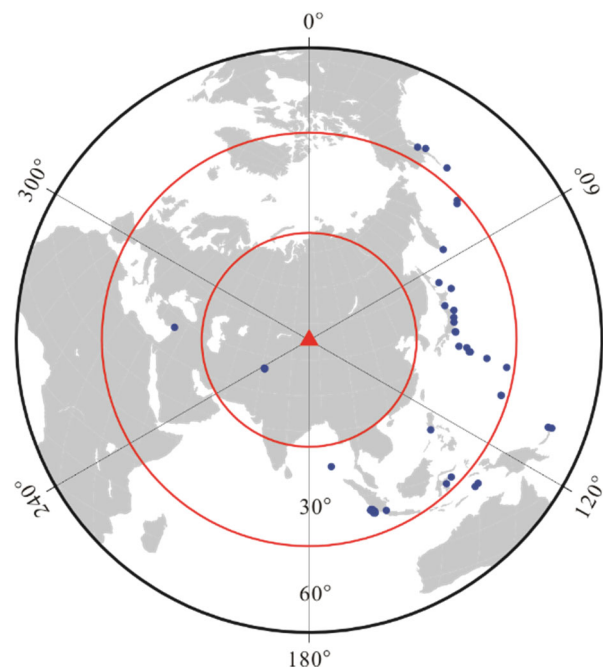

Figure 3. Distribution of teleseismic events. The red triangle denotes the center of our study region; the blue circles show the location of each seismic event used in this study.

Tracking and identification of PS converted wave along the profile was carried out. When the records in *R-T-Z* coordination for all stations of the earthquake are obtained, the waveform comparison diagram of each component of the profile can be constructed. Usually it is mainly the waveform of the *R* component (the optimal component obtained in all-directional polarization analysis). On the comprehensive comparison diagram of the *R* component (Fig. 4), we can distinguish some outstanding amplitude and the PS wave group with the time difference. Some can achieve reliable phase identification, based on the characteristics of time difference, amplitude and polarization.

The condition of phase identification is that the time difference of the same phase of PS wave on the adjacent stations is less than half of the PS wave apparent period. Generally, the apparent period of the teleseismic PS wave record is about 1 s, and the apparent velocity is close to or greater than 10 km/s. In this way, the phase tracking and identification of PS wave can be realized if the distance between adjacent two-stations is not greater than 5 km. When the intersection angle of the epicenter and the profile is larger, the PS wave, which has a greater apparent velocity, can realize the phase identification, even if the distance is more than 5 km.

The gravitational and aeromagnetic data were derived from a Bouguer gravity anomaly map (using a scale of 1 : 200 000) and an aeromagnetic anomaly map of Xinjiang (using a scale of 1 : 200 000; Zhao et al., 2008b), respectively (Fig. 5). The original data were decomposed using high-, band- and low-pass filtering techniques, with clearly anomalous aeromagnetic data being considered as representative of distinct geological bodies at different burial depths. The sampling interval vis-à-vis the original data was 5×5 km. High-pass filtering for short wavelength anomalies was conducted for up to three 5×5 km intervals (<15 km), band-pass filtering for intermediate wavelengths was conducted for between four and ten 5×5 km intervals (20–50 km), and low-pass filtering for long wavelengths was conducted for ten 5×5 km intervals and above (>50 km). In general, small bodies at shallow depths may generate short wavelength anomalies, whereas long wavelength anomalies may reflect the presence of deep, large bodies.

2.2 Seismic Technique

Seismic converted wave exploration is a deep probe technique (Shao et al., 2013). Its basic principle is diagrammatized in Fig. 6. With this method, we obtained the velocity structures, interfaces and faults at depths from the upper crust to the uppermost mantle. Because of the nearly vertical seismic rays of converted waves, this method has the advantage in imaging basement undulations and faults with steep gradients. First, we separated the interference waves with different polarization directions from one another, as proposed by Gal'perin (1975). Waveform inversion was then applied to obtain the velocity structure (Pan et al., 1988). To gain the modal function for structures where one layer overlay a half-space layer, we determined nine kinematic and dynamic parameters using the densities of the two layers (ρ_1 and ρ_2), the velocities of their P-waves (α_1 and α_2), the velocities of their S-waves (β_1 and β_2), the thickness of the upper layer (h_1), and the quality factors of the P-waves and S-waves of the upper layer (Q_{p1} and Q_{s1}). The number of parameters was decreased using the following empirical equations (Birch, 1961)

$$\rho=0.256+0.379\alpha \tag{1}$$

$$\begin{cases} Q_p = 14\alpha^2 \\ Q_s = 4Q_p \end{cases} \tag{2}$$

We selected parameters α, β and h as our independent variables because they exert a greater influence than parameter ρ.

To corroborate the P-wave velocities of the upper crust and upper mantle we obtained, we cross-checked them using a further three empirical equations, in which we selected α and K as the parameters of the initial model (Shao et al., 2013). We defined our modeled vector m as

$$m=(\alpha_1, K_1, h_1,…, \alpha_i, K_i, h_i,…, \alpha_n, K_n, h_n) \tag{3}$$

where α_i, K_i and h_i are the velocity of the P-wave, the V_p/V_s ratio, and the thickness of the ith layer, respectively.

As for the selection and design of the algorithm, the Haskell matrix algorithm was applied to the forward calculation of S_f (t, m) (Aki and Richards, 1980). The objective inversion function was expressed as
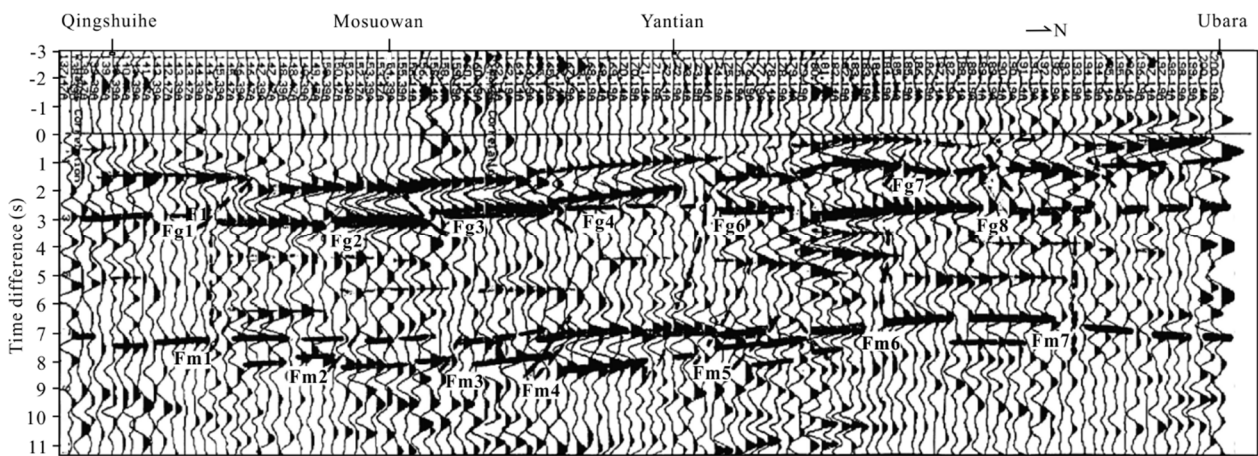

Figure 4. Phase discrimination of converted wave along the profile from Qingyijing to Ubara. Fg. Fault which cut through crystalline basement; Fm. fault which are cut through Moho discontinuity.
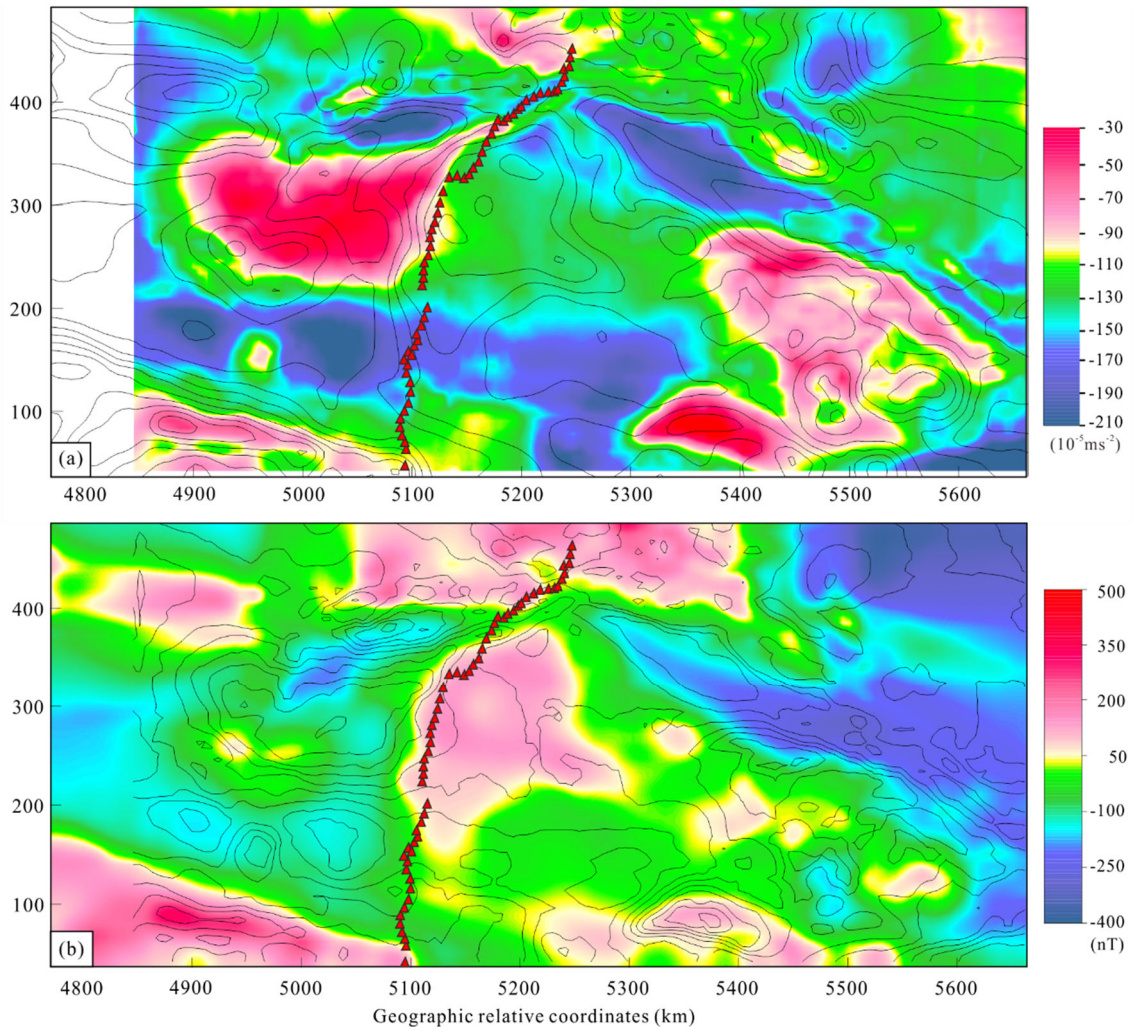
Figure 5. Gravitational data (color image with a background of aeromagnetic contour) (a) and aeromagnetic data (color image with a background of gravitational contour) (b) of the Junggar Basin.
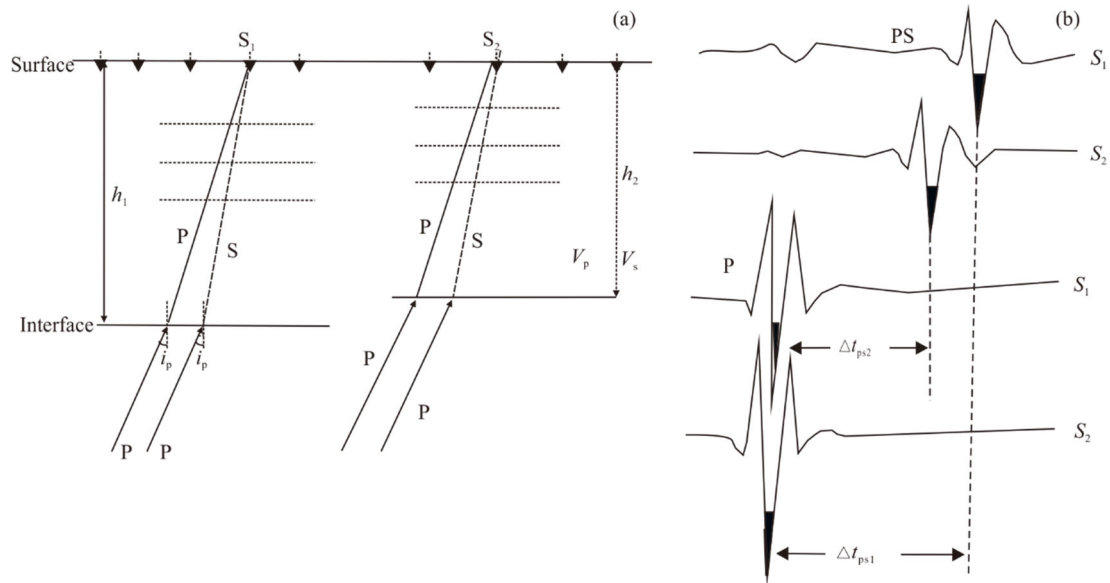

Figure 6. A schematic diagram showing the methodologic principle behind seismic converted wave exploration. (a) The ray paths of direct waves and PS converted waves; (b) the arrival time difference between PS converted waves and first pulse arrivals. P. P wave; S. S wave; i_p. P wave incidence angle; h_1, h_1. depths of the interfaces; S_1, S_2. seismic stations on the surface; PS. PS converted wave; S_1, S_2. converted waves from P wave; t_{ps1}, t_{ps2}. arrival time difference between PS converted waves and first pulse arrivals.

$$\varphi(m) = \int_0^{t_w} \left[S(t) - S_f(t, m) \right]^2 dt \tag{4}$$

where $S(t)$ is the recorded seismogram, $S_f(t, m)$ is the theoretical seismogram, and the modeled vector is m. The solution m satisfies Eq. (4) and the boundary conditions when

$$m_1 \leq m \leq m_2 \tag{5}$$

where m_1 and m_2 are the minimal and maximal reasonable values of the modeled parameters, respectively. Then the objective function

$$\varphi(m, v_k) = \varphi(m) - v_k \sum_{i=1}^{L} \ln \left| (m_i - m_{1i})(m_i - m_{2i}) \right| \tag{6}$$

was calculated using v_k as an arbitrary real value, and

$$v_1 > v_2 > \cdots > v_k > \cdots 0, \quad \lim_{k \to \infty} v_k = 0 \tag{7}$$

where L is the dimension of the model space; m_i, m_{1i}, m_{2i} are the ith model parameter and its lower and upper bounds.

A method combining boundary conditions, simplex and penalty techniques can be used to resolve the inverse problem (Wang, 1977). After obtaining a time profile by separating interference waves and building a velocity profile using the inversion method, the depth of the interface (h) can be calculated using the following equation

$$h = \frac{\Delta t_{PS} \cdot \overline{V_p}}{\sqrt{\overline{K}^2 - (C \overline{V_p}^2)} - \sqrt{1 - (C \overline{V_p}^2)}} \tag{8}$$

where ($\overline{V_p}$) and $\overline{K}$ are the mean values of the P-wave velocity and the V_p/V_s ratio above the interface, respectively.

2.3 Joint Inversion of Gravity and Aeromagnetic Data

The Bouguer anomaly $\Delta g(r_0)$ at r_0 was expressed by Rasmussen and Pedersen (1979) as

$$\triangle g(r_0) = -G \triangle \sigma \sum_{i=1}^{N} Z \cdot n_i \left[l_1(Y_2, i) + l_1(Y_2, i) \right] \tag{9}$$

where $l_1(Y, i) = Y \ln \dfrac{u_{i+1} + R_{i+1}}{u_i + R_i} + u_{i+1} \ln \dfrac{R_{i+1} + Y}{r_{i+1}} - u_i \ln \dfrac{R_{i+1} + Y}{r_i} -$

$w_i[\tan^{-1} \dfrac{u_{i+1} R_{i+1} + r_i^2}{Y w_i} - \tan^{-1} \dfrac{u_{i+1} R_{i+1} + r_i^2}{Y w_i}]$, $\quad \varphi_i = \tan^{-1} \left(\dfrac{\Delta z_i}{\Delta x_i} \right)$,

$\Delta x_i = x_{(i+1)} - x_i$, $\Delta z_i = z_{(i+1)} - z_i$, $x \cdot n_i = \sin\varphi_i$, $z \cdot n_i = -\cos\varphi_i$, $\omega_i = -x_i \sin\varphi_i + z_i \cos\varphi_i$, $u_i = x_i \cos\varphi_i + z_i \sin\varphi_i$, $u_{i+1} = x_{i+1} \cos\varphi_i + z_{i+1} \sin\varphi_i$, $r_i = (u_i^2 + \omega_i^2)^{1/2}$, $r_{i+1} = (u_{i+1}^2 + \omega_i^2)^{1/2}$, $R_i = (u_i^2 + \omega_i^2 + Y^2)^{1/2}$ and $R_{i+1} = (u_{i+1}^2 + \omega_i^2 + Y^2)^{1/2}$.

G is the gravitational constant, $\Delta\sigma$ is the density contrast, i is the ith polygonal node, and x_i and z_i are the coordinates for that node. We adopted a symmetrical 2.5D body in this study, i.e., $Y_1 = -Y_2 = Y$.

The three components of the magnetic anomaly were evaluated as

$$X_a(r_0) = -\sum_{i=1}^{N} x \cdot n_i \left[J_x I_x(i) + J_y I_y(i) + J_z I_z(i) \right] \tag{10}$$

$$Y_a(r_0) = -\sum_{i=1}^{N} \left\{ x \cdot n_i J_x I_y(i) - J_y \left[x \cdot n_i J_x I_y(i) + z \cdot n_i J_z I_y(i) \right] \right\}$$

$$+ z \cdot n_i J_z I_y(i) \tag{11}$$

and

$$Z_a(r_0) = -\sum_{i=1}^{N} z \cdot n_i \left[J_x I_x(i) + J_y I_y(i) + J_z I_z(i) \right] \tag{12}$$

hence the total magnetic anomaly can be written as

$$\Delta T(r_0) = X_a \cos A_0 \cos D_0 + Y_a \cos A_0 \sin D_0 + Z_a \sin A_0 \tag{13}$$

where $I_x(i) = I_2(Y_2, i) - I_2(Y_1, i)$, $I_y(i) = I_3(Y_2, i) - I_3(Y_1, i)$, $I_z(i) = I_4(Y_2, i) - I_4(Y_1, i)$,

$$I_2(Y, i) = \cos\varphi_i \ln \frac{(Y + R_i)r_{i+1}}{(Y + R_{i+1})r_i} - \sin\varphi_i \left[\tan^{-1} \frac{u_{i+1} Y}{w_i R_{i+1}} - \tan^{-1} \frac{u_i Y}{w_i R_i} \right]$$

$$I_3(Y, i) = \ln \frac{(u_{i+1} + r_{i+1})(u_i + R_i)}{(u_{i+1} + R_{i+1})(u_i + r_i)} \quad \text{and}$$

$$I_4(Y, i) = \sin\varphi_i \ln \frac{(Y + R_i)r_{i+1}}{(Y + R_{i+1})r_i} + \cos\varphi_i \left[\tan^{-1} \frac{u_{i+1} Y}{w_i R_{i+1}} - \tan^{-1} \frac{u_i Y}{w_i R_i} \right]$$

where J is the magnetic intensity; $J_x = J \cos A_1 \cos D_1$; $J_y = J \cos A_1 \sin D_1$, $J_z = J \sin A_1$; A_0 and D_0 in Eq. (13) are the aeromagnetic inclination and declination, respectively; and A_1 and D_1 are the magnetic dip angle and azimuth of the magnetization direction within the x-y plane, respectively.

The LSQR technique was used to establish the joint inversion of both datasets. However, as this method cannot well resolve the interfaces in a vertical direction (e.g., the Moho discontinuity), the initial model (i.e., the coordinates of x_i and z_i) was derived from the seismic results. In other words, the geometries of such interfaces were fixed during the inversion process. Taking into account the generally poor resolution in the uppermost mantle, many fewer polygons were added to the initial model. In addition, we manually checked the final results to avoid unreliable strong variations between the lower crust and the uppermost mantle. For more details, please refer to Zhao et al. (2017).

3 RESULTS
3.1 Velocity of the Crust and Uppermost Mantle in Western Junggar Basin

After data processing (Shao et al., 2013; Shao and Zhang, 1999) and comprehensive geological interpretation, a 2D velocity structure of the crust and uppermost mantle was obtained (Fig. 7).

Ten interfaces were identified, of which seven were stable, i.e., A_1, A_2, B, G, C_1, C_2 and M (Fig. 7). Comparing these results with those obtained during oil and gas prospecting (i.e., seismic near-vertical reflections) (Zhao, 1992), we were able to attribute interface A_1 to the Jurassic. A_2 appeared related to the low velocity zones observed within Triassic to Permian layers. Interface B was taken to represent top surface of the Basin's folded Hercynian-age basement. Interface G marked the top surface of the crystalline basement. Interfaces C_1 and C_2 were interpreted as representing the bases of the upper and middle crust, respectively. Interface M (the Moho discontinuity) was taken to mark the base of the crust.

Along the profile Interface B deepens southward at a stable rate, from a depth of 1–2 km in the Hongyan step-fault zone, to 12–16 km in the Changji depression (Fig. 7). The folded surface of the basement and the crystalline basement beneath it merge together. Further south, in the uplift belt of the foreland of the northern Tianshan, the thickness of the folded Hercynian-age basement increases greatly.

Interface B appears deeper than the top surface of the Carboniferous by ~2 km in the Changji depression and the Mosuowan uplifted areas; this result was obtained by comparing the top surface of the Carboniferous layer with that of Interface B using the seismic converted wave method. Here, the buried depth of Interface B appears to control, to a large degree, the thickness of the Permian layer, which can be as thick as 4–6 km in the Changji depression area.

The first of the more closely converted interfaces below Interface B is Interface G (the top surface of the crystalline basement). Interface G can be well traced along the profile. Of the interfaces below Interface B, Interface G is the converted wave intracrustal interface exhibiting the strongest energy profile, except for the Moho. The energy changes laterally, indicating a serious lateral variation in wave impedance on the interface. In the southern part of the profile, where the folded basement deadens out and the deposited sedimentary cover merges with Interface G, the energy emitted by Interface G's converted waves is very strong; an example of this can be seen in the converted wave profile for the Changji depression (Zhao et al., 2010). In the northern part of the profile where the interfaces B and G exist together, the energy of the converted waves from Interface G is weak, due to Interface G's reduced wave velocity contrast. The velocity near Interface G is ~V_p=6.0 km/s, while the velocity of the folded basement is generally ~V_p=4.8–5.0 km/s. This large difference in wave velocity is responsible for these strong converted wave phases. The characteristics of Interface G are almost identical to those of the top interface of the crystalline basement observed in most regions of China, such as in the Tianshan (Zhao et al., 2003), the Tarim Basin (Zhao et al., 2006) and northern China (Zhang et al., 2009). Interface G can therefore be taken as the top surface of the crystalline basement along the profile, with the thickness between interfaces B and G representing the thickness of the folded basement.

The overall depth of Interface G is shallower to the north and deeper to the south, increasing from 8 km in the northern part of the profile (i.e., the Kalameili Hercynian marginal accretionary belt) to 13–14 km at the profile's southern end (i.e., the Changji depression; see Fig. 7). Several faults cutting through the crystalline basement are located along the profile, forming several rectangular blocks of different sizes. The buried depths of each block are different. There are four uplifted belts along the profile, i.e., the Mosuowan uplifted belt, Lunnan high, Sangequan high and Shiyingshan high from south to north. In the Mosuowan uplifted belt, the depth of Interface G is shallower, being 5–6 km, but it increases to ~6–7 km beneath the Suosuoquan area. The buried depth of Interface G is 7–11 km in the middle uplifted belts, and 9–10 km under the southern belts. The formation of these uplifted belts along Interface G could be the result of the control exerted by, and movement of, the deep faults located on either side of the uplifted belts. The regions between the uplifted belts take the form of depressions; these are covered by thick sedimentary deposits and are the principal areas where oil-producing strata were first found.

It is notable that an angular unconformity exists within the top surface of crystalline basement G and the base of the folded basement, causing the thickness of the folded basement to reduce southward.

Interface C_1 is the top interface of the middle layer of the crystalline crust; it is a stable, traceable, converted and reflected interface within the crystalline crust. It appears similar in form to Interface G, with a gently sloping buried depth of 24–28 km. In earlier studies, this interface was taken to be the top surface of the Precambrian crystalline basement (Zhang and Chen, 1998). Although Interface C_1 can be clearly and rationally identified as stable, the layer's wave velocity can be as high as 6.6–7.0 km/s. Interface C_1 is therefore more likely to represent the top surface of the middle layer of the crystalline crust rather than the top surface of the Precambrian crystalline basement.

Interface C_2, with a gently sloping buried depth of 31–35 km, could reasonably be taken to represent the base of the middle crustal layer, being a more stable converted and reflected interface within the crystalline crust. In the piedmont areas of the Tianshan, the depth of Interface C_2 is ~36 km. Interfaces C_1 and C_2 have a similar undulating pattern, most likely forming the top and bottom surfaces of the middle crustal layer, respectively.

At the bottom of the crust, the Moho represents a strongly converted and reflected regional interface almost parallel to Interface C_2. However, the detailed geometry of this interface changes greatly along the profile, because it may be cut across by up six deep faults (Fm1 to Fm6 in Fig. 5). A sizeable uplifted belt has developed in the northern part of the profile, where the upper boundary of the uplifted belt can be measured at a subsurface depth of ~44 km. To the south, the depth of the Moho increases gradually to ~52 km at the southern end of the profile. The faults cutting across the Moho (e.g., Fm1 to Fm5) cause Moho uplift at different degrees, demonstrating that the Moho's tectonic is related to these faults.

3.2 Density and Magnetization Intensity along the Profile

According to the 1 : 200 000-scale Bouguer gravity anomaly map of Xinjiang (Zhao et al., 2008b), there are two gravity gradient zones, one along the northern, and one along the southern, margins of the Basin, both of which clearly delineate the shape of the Basin. This matches with the region's topographical and geological frameworks. The magnetization intensity of th rock, together with P-wave velocity and density, can be used to distinguish rock types. The aeromagnetic anomaly map of Xinjiang (scale 1 : 200 000; Zhao et al., 2008b) shows a stronger magnetism in the southern part of the Basin (i.e., the Manasi terrain) than in the rest of the Basin. Based on the P-wave velocity structure and the faults investigated at the surface, a starting model for the density in each cell was constructed using the following velocity-density relation (Eq. 14; Feng et al., 1986)

$$\rho = \begin{cases} 2.78 + 0.56(V_p - 6.0), & 5.5 \le V_p \le 6.0 \\ 3.07 + 0.29(V_p - 7.0), & 6.0 \le V_p \le 7.5 \\ 3.22 + 0.20(V_p - 7.5), & 7.5 \le V_p \le 8.5 \end{cases} \quad (14)$$

The resultant 2D density and magnetization intensity models of the crust and uppermost mantle along the profile are shown in Figs. 8, 9, respectively. Figure 8 indicates that, within the region, the density distribution exhibits differing vertical and horizontal characteristics. Vertically, the density value increases with depth. Horizontally, a higher middle crustal density was detected in the northern part of our profile. Densities are lower

in the lower crust in the center of the region. Along the profile, the density in the uppermost mantle is much higher in the central Basin (i.e., 3.32 g/cm³) than at the southern end of the profile (where it averages 3.11 g/cm³).

Figure 9 shows that the magnetization intensity is higher at shallower depths than at deeper depths, with the highest values occurring within the upper crust. Horizontally, the magnetization intensity increases northward, but the strongest values are seen in the middle of the profile; these values exhibit a strongly positive correlation with the velocity and the density values along the profile.

Based on the results mentioned above, we know that the joint inversion of gravity with aeromagnetic data not only gives a clearer understanding of the 2D density and magnetization intensity structures of the crust and uppermost mantle along the profile, but also that it can contribute to determination of the dif-

ferent spatial depths of different faults and the corresponding relation between deep and shallow faults.

4 DISCUSSION AND CONCLUSION
4.1 Layered Structures

Using the differences in physical parameters within different layers, the crust of this region can be divided into three tectonic layers: a deposited sedimentary cover; a folded basement; and a crystalline basement. In addition, each of these three tectonic layers can be subdivided into several sublayers due to the existence of some obvious interfaces within these tectonic layers. The deposited sedimentary cover can be subdivided into three tectonic sublayers, i.e., the Jurassic tectonic layer (J), the Triassic tectonic layer (T) and the Permian tectonic layer (P).
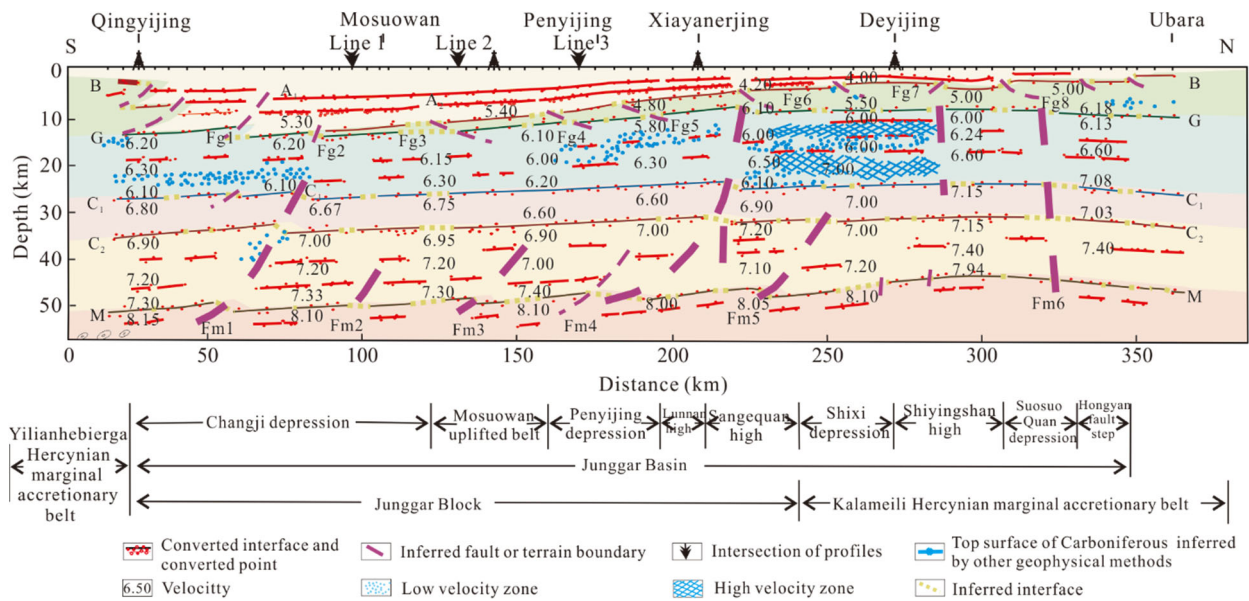

Figure 7. 2D velocity structure of the crust and uppermost mantle along the profile from Qingyijing to Ubara.
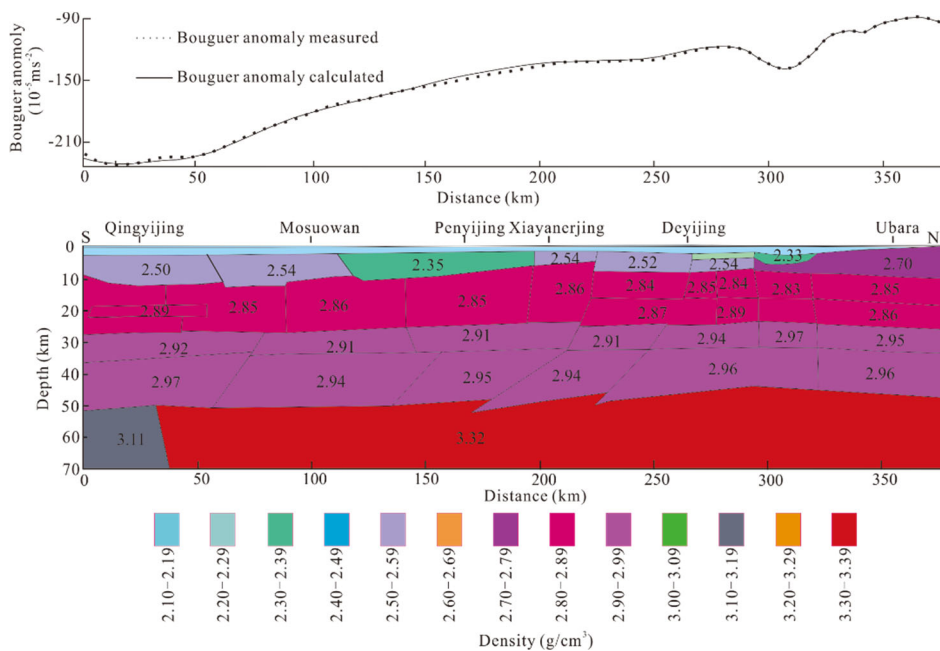

Figure 8. 2D density structure of the crust and uppermost mantle along the profile from Qingyijing to Ubara.
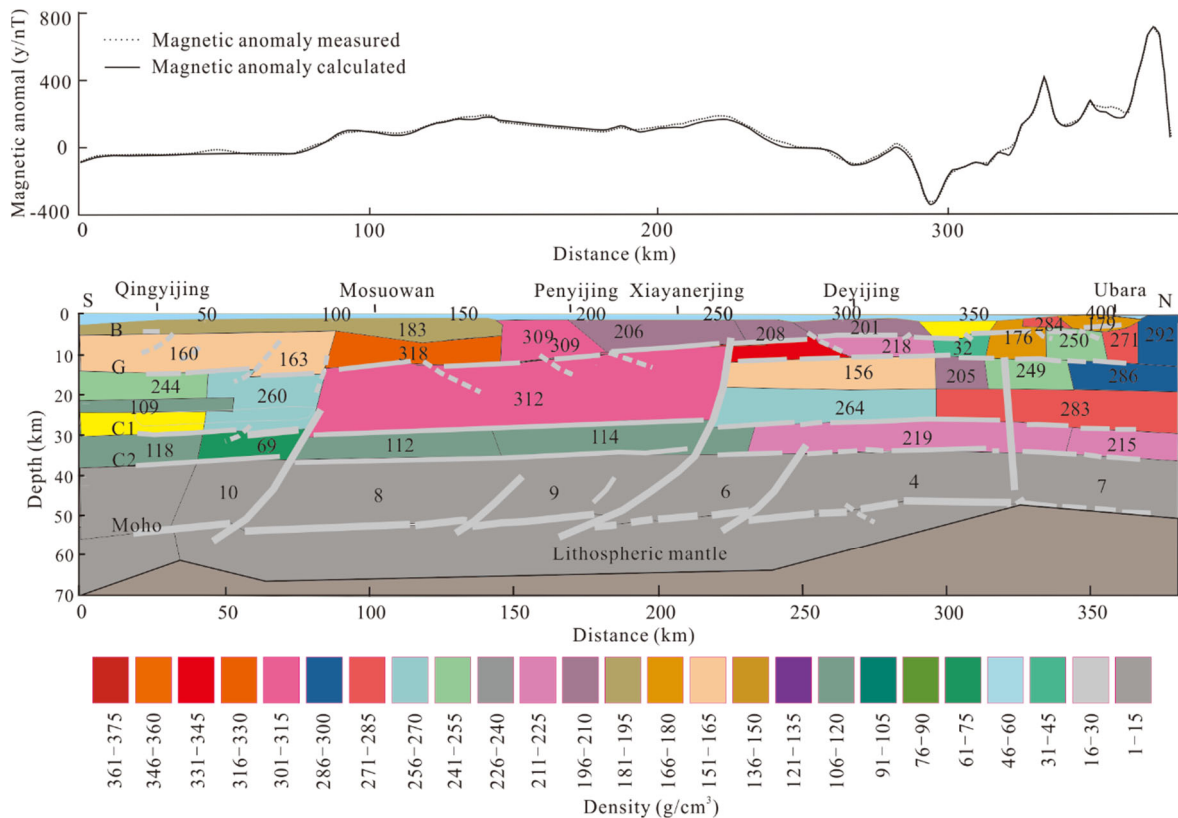
Figure 9. 2D magnetization intensity structure of the crust and uppermost mantle along the profile from Qingyijing to Ubara.

The folded basement can be subdivided into two tectonic sublayers, i.e., the Carboniferous and Devonian (C+D) Hercynian tectonic layer and the Caledonian tectonic layer. The crystalline crust can be subdivided into the upper, middle and lower layers of the crystalline crust. The top two tectonic layers and the upper layer of the crystalline crust are often called the 'upper crust'.

4.1.1 Deposited sedimentary cover (upper tectonic layer)

The thickness of the deposited sedimentary cover in this region is ~0–14 km. The converted interfaces A1 and A2 divide the deposited sedimentary cover into the upper, middle and lower sublayers. Even though the parameters of each sublayer have in the past been described by seismic prospecting, the thickness of the lower (Permian) layer obtained using wave conversion is greater in some regions than the thicknesses obtained from present seismic reflectivity measurements.

4.1.2 Folded Paleozoic basement (middle tectonic layer)

This layer was the principal focus of this research. It is located between the converted interfaces B and G, and can be defined by the values of physical parameters such as the P-wave velocity (4.6–5.7 km/s) and density (δ=2.64 g/cm^3 in the inner Basin, and δ=2.50–2.62 g/cm^3 in the western Basin). Its magnetization intensity is H=2.0–2.9 A/m, which is relatively high. Due to an angular unconformity which exists between interfaces B and G in a south-north direction, the thickness of the Paleozoic basement decreases southward, from 8–10 km in the Hongyan fault-step zone, to 0–1 km in the Changji depression. In the marginal regions of the Basin, the thickness of the crystalline basement increases due to the thrusting and napping between the

Basin and its surrounding mountains. The thickest parts of the basement occur along the northern and southern margins of the Basin. In the uplift region in the northern Tianshan piedmont, the thickness of the basement is >10–14 km. The thrusting and napping of the surrounding mountains are responsible for the basement thickening. The thickness of the basement decreases from north to south, indicating that the crystalline crust in the southern part of the folded basement was uplifted during the Paleozoic, a process which was followed by the erosion of the folded basement and its subsequent depression, after which it experienced heavy sedimentary deposition prior to a Late Permian uplift.

Additionally, the thickness of the basement changes abruptly at the Sangequan high. The thickness is 3–5 km in the north, and 2–3 km in the south. Furthermore, the P-wave velocity of the northern block is higher than that of the southern block. In the north, the top surface of the crystalline basement symmetrically mirrors the Moho, while in the south the two have an undulating synclinal relation. Based on the features mentioned above and combining these with observed differences in electrical values, the faults and the serpentine suites near these faults (Xiao and Tang, 1992), it can be inferred that a crustal collision orogenic belt may exist along the Sangequan uplifted belt.

4.1.3 Crystalline crust (lower tectonic layer)

The lower tectonic layer can also be subdivided into three tectonic sublayers (i.e., an upper, middle and lower sublayer). The sublayer between interfaces G and C_1 is the upper tectonic layer; that between interfaces C_1 and C_2, the middle tectonic layer; and that between interfaces C_2 and the Moho, the lower tectonic layer.

(1) The upper sublayer of the crystalline crust

This layer can be further subdivided into two secondary sublayers according to the velocity and interface structures present within each layer. The upper secondary sublayer is a low P-wave velocity zone with V_p=5.85–6.0 km/s. This low P-wave velocity zone may be related to detachment and sliding planes within the crystalline crust. The P-wave velocity of the layer in the region to the north of the Sangequan high peaks at 6.1–6.6 km/s, possibly related to magma intrusion or rock effusion. The lower secondary sublayer exhibits a stable P-wave velocity distribution, with values of V_p=6.2–6.45 km/s, and a corresponding density of δ=2.76–2.80 g/cm^3. In the region to the north of the Sangequan high, the P-wave velocity of this sublayer is as high as V_p=6.5–6.7 km/s. The thickness of the upper layer of the crystalline crust changes little due to the parallel positioning between interfaces G and C.

(2) The middle sublayer of the crystalline crust

The middle sublayer of the crystalline crust is located between interfaces C_1 and C_2. Interface C_2 is almost synclinal with interface C_1, causing the thickness of the middle sublayer of the crystalline crust to change little, averaging between 6–8 km. The P-wave velocity of this layer is relatively high, with a V_p of 6.6–6.8 km/s. The corresponding density is 2.80–2.85 g/cm^3, and the magnetization intensity 1.9 A/m.

In the region north of the Sangequan uplifted belt the P-wave velocity increases quickly to V_p=6.9–7.1 km/s, which is almost the same as that of the lower crust in most regions of China. This may in turn account for the high strength of the crystalline crust in this region.

In the Zayi'er Mountains to the west of the Kalameili belt, a low velocity zone with a P-wave velocity of 6.1–6.3 km/s and a density of ~2.70 g/cm^3 has developed. A body with a high magnetization intensity (>3.0 A/m) has developed in the upper and middle crustal layers of the Basin, over a range of 200 km in an E-W direction, 180 km in a N-S direction, and 8–45 km in depth.

(3) The lower sublayer of the crystalline crust

This sublayer is located between interfaces C_2 and G. The geometry of interface C_2 is basically parallel to that of the Moho. The density of this layer is 2.85–2.90 g/cm^3, averaging 2.87 g/cm^3, and its magnetization intensity is 1.2 A/m. The P-wave velocity of this lower sublayer of the crystalline crust presents as a gradient, from 6.8–7.0 km/s at the sublayer's top surface to 7.3–7.4 km/s at its base.

Two lower velocity anomalies were detected in the lower sublayer of the crystalline crust. To the north of the Sangequan uplifted belt, the P-wave velocity increases abruptly to 7.0–7.4 km/s. As a general rule, the lower sublayer exhibits a high P-wave velocity, a high density and little variation in layer thickness, accompanied by weak deformation under strong compression from the Basin's margins. All of these features would indicate that the crystalline crust of the Basin is more rigid and stable than those found in other regions of China.

(4) The uppermost mantle

The P-wave velocity near the Moho is relatively stable, where V_p=8.00–8.15 km/s and δ=3.11–3.32 g/cm^3. The P-wave velocity in the southern part of the Basin is higher (i.e., at 8.10–8.15 km/s）than corresponding values for its northern part (8.05–8.10 km/s), but the P-wave velocity in the Shiyingshan high exhibits the lowest values (7.94–8.00 km/s).

4.2 Inferences for Basement Rock Types in the Western Junggar Basin

The basement properties of the Junggar basement can be inferred based on the relations between velocity, density and rock properties (Liu and Wu, 1997; Fig. 10) and the corresponding basement P-wave velocity, which can be determined using two seismic wide-angle reflection/refraction profiles, and taking into account the profiles from Xayar to Burjing (Zhao et al., 2003) and from Emin to Qitai (Zhao et al., 2010). Results are shown in Table 1.
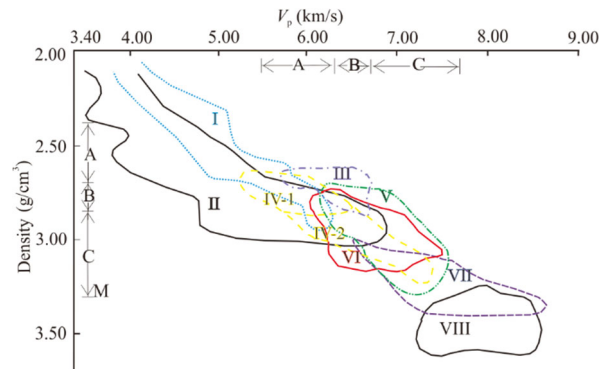
Figure 10. Determining rock types at depth based on velocity and density. I. Sandstone; II. basalt; III. granite; IV-1. intermediate-acid schist, gabbride; IV-2. intermediate-basic schist, gabbride; V. granulite; VI. gabbro; VII. peridotite; VIII. eclogite.

Table 1 Basement property parameters along the profile from Qingyijing to Ubara

Range (km)		0–50	50–120	120–200	200–240	240–270	270–310	310–350	350–400
Velocity (km/s)	Upper layer				4.80	4.20	5.50	5.00	5.00
	Lower layer	6.20	6.20	6.15	5.80	6.10	6.00	6.00	6.18
Density (g/cm^3)	Upper layer				2.45	2.50	2.61	2.60	2.60
	Lower layer	2.75	2.76	2.75	2.76	2.74	2.74	2.73	2.75
Magnetic	Upper layer								
intensity (A/M)	Lower layer	154	154–200	306–311	312	314	32–224	176	271–292
Rock type	Upper layer				I	II	I	I	I
	Lower layer	III, II, IV-1, V, VI	III, II, IV-1, V, VI	III, II, IV-1, V, VI	II, II, IV-1	I, II, IV-1	I, II, IV-1	II, I, II, IV-1	II, I, II, IV-1, VI

I. Sandstone; II. basalt; III. granite; IV-1. intermediate-acid schist, gabbride; IV-2. intermediate-basic schist, gabbride; V. granulite; VI. gabbro; VII. peridotite; VIII. eclogite.

These results would indicate that the basement rocks of the southern Basin are very complicated, and that acidic, basic and ultra-basic rocks coexist, along with a granitic, basaltic and granulate mix. Additionally, the isotope assay for the post-collision intermediate-acid plutonic rocks of the Basin measured using analyses of Pb (Kwon et al., 1989), Nd and Sr (Hopson et al., 1989) isotopes, shows that these intermediate-acid plutonic rocks are all from oceanic-mantle depositional layers, or from oceanic volcanic rocks. In other words, they are not derived from the Precambrian basement or the paleo-continental crust.

The exposed Precambrian rocks found along the Basin's margins were not identified until recently. The exposed rocks distributed throughout the region have traditionally been identified as of Late Cambrian oceanic origin, or as the remains of Middle Cambrian deposits. In the Silurian turbidites found to the south of the Kalameili fault, the direction of the Paleozoic floats indicated by the imbricated gravel and the scour channel mode is from south to north, indicating that land blocks older than the Silurian were most likely the source. The considerable maturity of the clasolite component and the presence of a few mafic volcanic lithics would also indicate that these rocks were sourced by an old craton. Both these findings would tend to suggest that the source region was not simply a small land block composed of Ordovician and/or Cambrian mafic volcanic lithics (Xiao and Tang, 1992).

The geological tectonic evolution of the Tianshan Mountains and Junggar Basin region endured four tectonic evolutionary phases: the Early Cambrian oceanic evolution of the Junggar (during which the Pan-Tarim Block split); the Late Cambrian oceanic evolution of the Junggar (during which the oceanic basin was formed by the extension and splitting of the Early Cambrian folded oceanic depositional basement from the Mid–Early Devonian to the end of the Middle Devonian); the residual oceanic basin phase (from the Late Devonian to the Middle Carboniferous); and the phase of inland mountain building after the collision of the Indian and Eurasian continental plates (Xiao and Tang, 1992). Large-scale crustal extension and splitting episodes have therefore occurred twice in the Junggar region, forming a two-term Junggar Ocean, one following the other. In the Late Cambrian Junggar Ocean period, some relatively small blocks existed, most of which were composed of deformed and metamorphic oceanic masses of Early Cambrian age; these small blocks were natural products resulting from the extension and splitting of the Early Cambrian folded basement.

Looking at the aeromagnetic anomaly map of the Junggar Basin (Fig. 5) (Zhao et al., 2008b), a relatively strong magnetism appears in the southern part of the Basin (i.e., the Manasi terrain), exhibiting an intensity similar to that of Precambrian gneiss, magmatic granite and hornblende schist. However, a joint inversion of gravity with aeromagnetic data would indicate that these rigid blocks were formed by paleo-rigid blocks or deep faults caused by north-south compression. All of these faults would have provided channels through which materials could have migrated from the mantle into the crust, subsequently intruding laterally along different strata within the crust. The region's crustal composition would therefore have been changed, or even reproduced, causing the high velocity, high density and high geomagnetic intensity crust we observed.

Based on the 1 : 200 000-scale gravity anomaly map of Xinjiang (Fig. 5) (Zhao et al., 2008b), there appear to be two gravitational anomaly gradients, one along the southern, and one along the northern, margin of the Basin. The aeromagnetic anomaly map shows the south of the Basin (i.e., the Manasi terrain) having a strong magnetism equivalent to values seen for Precambrian gneiss, migmatite, compound granite and amphibole-schist (Kuang, 1993). A steep gradient zone around the Basin was also detected on the Bouguer gravity anomaly map (Zhao et al., 2003); this gradient coincides with the Basin's topography, landforms and geological framework, and is indicative of a consistency between the Basin's crustal structure and surficial form. In the Xayar-Burjing geoscientific profile, velocity and density structures show that the crustal thickness is 47 km in the Basin, including a 15 km-thick sedimentary layer deposited since the Devonian, which itself contains an 11-km thick Mesozoic–Cenozoic layer. If the thickness of these sediments were to be subtracted from the crustal depth measured by the Xayar-Burjing geoscientific profile, the Basin's crystalline crust would be merely 32 km thick. Further, the density of the Basin's basement is 2.87 g/cm^3 in the Wulungu terrain, and 2.85 g/cm^3 in the Manasi terrain. The former has a P-wave velocity of 5.9 km/s, and the latter one of 5.8 km/s. This would tend to suggest that the two terrains which comprise the Basin may have different material compositions.

Extant geological and geophysical data indicate that the basement of the Basin is composed of two terrains which collided (i.e., the Manasi terrain in the south, and the Wulungu terrain in the north). It is a 'trough' basement composed of early Middle Paleozoic oceanic materials, but the possibility of the inclusion of some small, older land blocks within these materials cannot be excluded.

4.3 Geodynamic Problems Revealed by the Comprehensive Geophysical Profile

The N-S trending geophysical profile has located several faults, such as the Junggar southern marginal fault (Fm1), the Tuositai-Qitai fault (Fm2), the Lunnan fault (Fm3), the Tusituoyila fault (Fm4) and the Hongyan fault (Fm5). Most of these faults are insidious, i.e., they do not cut upward through the ground surface, but downward through the Moho. They therefore represent significant controls on the tectonic evolution of the Basin.

A thrust fault system has developed on the northern and southern sides of the Basin, where some nappes have thrust older layers into the surface, causing thrusting, napping and folding. The crust of the Basin along the profile is composed of three layers, i.e., the upper, middle and lower crustal layers, of which the middle layer is relatively thin.

Crustal characteristics (especially for the upper and middle crustal layers) change greatly along the profile. The Basin can be divided into northern and southern parts, with a boundary along the Lunnan fault. The Junggar Block located in the southern part of the Basin exhibits a more stable stratigraphy than the northern block. Even though some abnormal bodies with high velocity, high density and high magnetic intensity values have developed within the crust, the crust appears well layered, with clear stratigraphic layering.

Notably, a low velocity zone appears to have developed in the lower part of the upper crustal layer along the southern
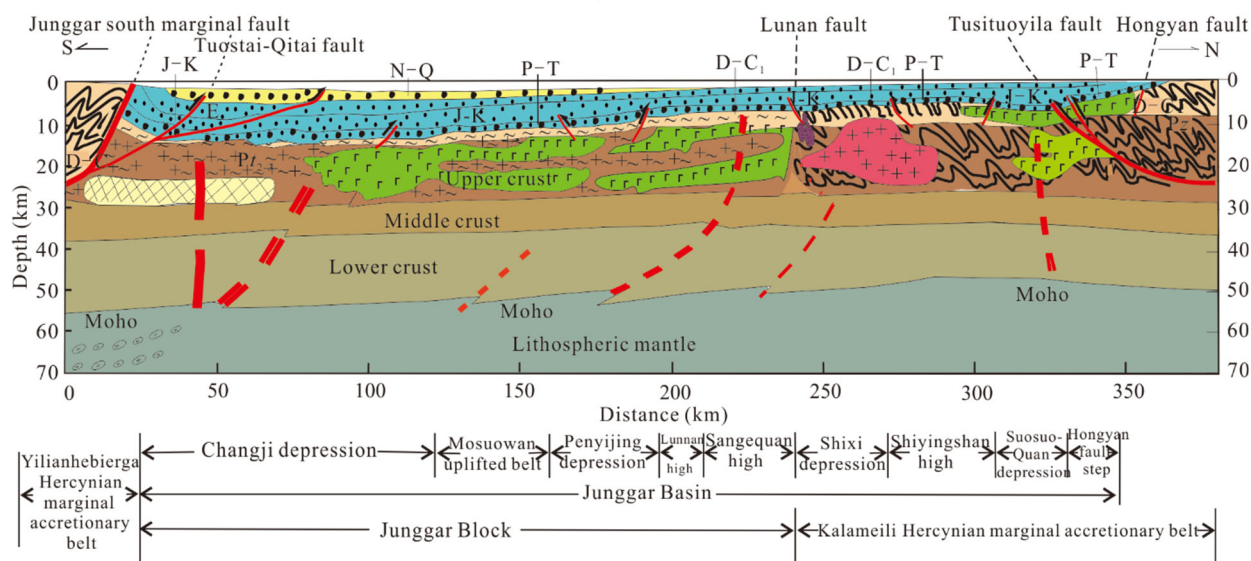
Figure 11. The geological interpretation for the western Junggar Basin along the profile from Qingyijing to Ubara.

margins of the Basin. This can be inferred as having resulted from the exchange of deep materials and the concomitant energy values with materials from the shallow part of the crust. The crust (especially the upper crustal layer) of the Hercynian Kalameili marginal accretion belt exhibits a relatively complicated structure, with some petrosilex intrusions of different chronologies and kinds.

The joint action of the thrusting of the Tusituoyila fault along the northern margins of the Basin and the depth of the Tusituoyila fault have produced not only a series of nappes and folds, but have also led to an exchange of materials and energy between the crust and mantle through this fault, giving rise to a highly complex tectonic environment along the Basin's northern margins.

Along the profile the lower crust is thicker in the southern and central sections of the profile, and shallower in the northern section. The thickness of the crystalline basement remains almost the same along the profile. The variation in the thickness of the lower crust appears to have been adjusted by some Moho dislocations at the base of the crust.

We developed a geodynamic interpretation (Fig. 11) based on the velocity (Fig. 7), density (Fig. 8), magnetic intensity (Fig. 9) and some tectonic analyses (Wu et al., 2018; Zhang et al., 2017; Li et al., 2017; Xu et al., 2016). Values rendered by the abnormal bodies widely distributed throughout the Basin. A double basement, a Hercynian folded basement and a paleo-crystalline basement appear to have developed along the profile (especially in its northern section). The thickness of the folded basement which falls between interfaces B and G (Fig. 7) decreases southward, consistent with the results of another profile across the Basin with a near E-W direction (i.e., the profile from Kalameili to Kamusite; Zhao et al., 2008a). However, the near E-W striking wide-angle reflection/refraction profile from Emin to Qitai (Zhao et al., 2013) located only on the paleo-crystalline basement, not on the Hercynian folded basement. Taking a consideration these differences, we suggest that the northern part of the Junggar Basin possesses a double basement, while the southern part has a single basement, i.e., a paleo-crystalline basement. The development of the double basement may indicate that the

northern Junggar Basin has experienced more complicated tectonic evolution.

REFERENCES CITED

Aki, K., Richards, P. G., 1980. Quantitative Seismology. Freeman W. H. and Company, New York

Birch, F., 1961. Composition of the Earth's Mantle. *Geophysical Journal Royal Astronomical Society*, 4: 295–311

Chen, S., Pe-Piper, G., Piper, D. J. W., et al., 2014. Ophiolitic Mélanges in Crustal-Scale Fault Zones: Implications for the Late Palaeozoic Tectonic Evolution in West Junggar, China. *Tectonics*, 33(12): 2419–2443. https://doi.org/10.1002/2013tc003488

Feng, R., Yan, H. F., Zhang, R. S., 1986. A Method and Programming for Quick Inversion of 3D Potential Field. *Acta Geologica Sinica*, 4: 390–402 (in Chinese with English Abstract)

Gal'perin, E. L., 1975. Polarization-Positional Correlation of Seismic Waves. *Dokl. Akad. Nauk*, 223(2): 336–334

Hopson, C., Wen, J., Tilton, G., et al., 1989. Paleozoic Plutonism in East Junggar, Bogdashan and Eastern Tianshan, NW China. *EOS Trans. Am. Geophys Union*, 70: 1403–1404

Huang, J. Q., 1979. On the Multi-Cyclic Development of Geosynclinals Fold Belt. *Science in China Series D: Earth Science*, 94: 384–397 (in Chinese)

Kuang, J., 1993. Tarrane Collage and the Formation and Evolution of the Junggar Basin. *Xinjiang Petroleum Geology*, 14(2): 126–132 (in Chinese with English Abstract)

Kwon, S. T., Tilton, G. R., Coleman, R. G., et al., 1989. Isotopic Studies

Bearing on the Tectonics of the West Junggar Region, Xinjiang, China. *Tectonics*, 8(4): 719–727. https://doi.org/10.1029/tc008i004p00719

Li, D., He, D., Lian, Y., et al., 2017. Structural Evolution and Late Carboniferous Magmatism of the Zhongguai Arc in the Western Junggar Basin, Northwest China: Implications for Tectonic Evolution of the Junggar Ocean. *International Geology Review*, 59(10): 1234–1255. https://doi.org/10.1080/00206814.2016.1160801

Liu, Y. G., Wu, X. G., 1997. Relation between Velocity and Rock Composition. *Chinese Journal of Geophysics*, 43(2): 211–220 (in Chinese with English Abstract)

Pan, G. S., Phinney, R. A., Odom, R. I., 1988. Full-Waveform Inversion of Plane-Wave Seismograms in Stratified Acoustic Media: Theory and Feasibility. *Geophysics*, 53(1): 21–31. https://doi.org/10.1190/1.1442397

Peng, X. L., 1994. The Evidence for Land Crust Existence in the Junggar Basin during Early Paleozoic. *Xinjiang Petroleum Geology*, 15(4): 291–297 (in Chinese with English Abstract)

Rasmussen, R., Pedersen, L. B., 1979. End Corrections in Potential-Field Modeling. *Geophysical Prospect*, 27(4): 749–760

Shao, X. Z., Zhang, J. R., 1999. Petroleum Prospecting and Deep Structure. *Petroleum Exploration and Development*, 26(2): 11–14 (in Chinese)

Shao, X. Z., Zhang, J. R., Fan, H. J., 2013. Seismic Converted Wave Exploration. Seismological Press, Beijing (in Chinese)

Wang, D. R., 1977. Solutions and Optimiaation of Nonlinear Equations. People's Education Press, Beijing (in Chinese)

Wang, F. Z., Yang, M. Z., Zheng, J. P., et al., 2002. Geochemical Evidence of the Basement Assembled by Island Arc Volcanic Terranes in Junggar Basin. *Acta Mineralogica et Petrologica*, 21(1): 1–10 (in Chinese with English Abstract)

Wang, G., Qin, Y., Shen, J., et al., 2018. Dynamic-Change Laws of the Porosity and Permeability of Low- to Medium-Rank Coals under Heating and Pressurization Treatments in the Eastern Junggar Basin, China. *Journal of Earth Science*, 29(3): 607–615. https://doi.org/10.1007/s12583-017-0908-4

Wu, S. C., Huang, R., Xu, Y. X., et al., 2018. Seismological Evidence for a Remnant Oceanic Slab in the Western Junggar, Northwest China. *Journal of Geophysical Research*: *Solid Earth*, 123(5): 4157–4170. https://doi.org/10.1029/2017jb015332

Xiao, X. C., Tang, Y. Q., 1992. Tectonics in Northern Xinjiang and Its Adjacent Regions. Geological Publishing House, Beijing (in Chinese)

Xu, Y. X., Yang, B., Zhang, S., et al., 2016. Magnetotelluric Imaging of a Fossil Paleozoic Intraoceanic Subduction Zone in Western Junggar, NW China. *Journal of Geophysical Research*: *Solid Earth*, 121(6): 4103–4117. https://doi.org/10.1002/2015jb012394

Yan, W. B., Wang, G. C., Li, L., et al., 2015. Deformation Analyses and Their Geological Implications of Carboniferous–Permian Tectonic Transition Period in Northwest Margin of Junggar Basin. *Earth Science*, 40(3): 504–520. https://doi.org/10.3799/dqkx.2015.040 (in Chinese with English Abstract)

Yang, K. M., 1992. Formation and Evolution of the Basins in Northwestern China. *Northwestern Geology*, 13: 1–6 (in Chinese with English Abstract)

Yang, Y. Q., Qiu, L. W., Cao, Y. C., et al., 2017. Reservoir Quality and Diagenesis of the Permian Lucaogou Formation Tight Carbonates in

Jimsar Sag, Junggar Basin, West China. *Journal of Earth Science*, 28(6): 1032–1046. https://doi.org/10.1007/s12583-016-0931-6

Zhang, K., 1991. On the Division, Drift, Collision and Convergence of Land Blocks and the Evolution of Petroleum Basins of China. *Xinjiang Petroleum Geology*, 12(2): 91–106 (in Chinese with English Abstract)

Zhang, X. K., Duan, Y. H., Zhao, J. R., 2009. Crustal Structures and Their Tectonic Implications in Different Tectonic Block Regions of the Chinese Mainland. *Earthquake Science*, 22(4): 337–356. https://doi.org/10.1007/s11589-009-0337-2

Zhang, Y. J., Chen, J. X., 1998. Geological Structure, Evolution and Classification of the Junggar Basin. *Acta Geologica Sinica*, 22: 12–23 (in Chinese with English Abstract)

Zhang, S., Xu, Y. X., Jiang, L., et al., 2017. Electrical Structures in the Northwest Margin of the Junggar Basin: Implications for Its Late Paleozoic Geodynamics. *Tectonophysics*, 717: 473–483. https://doi.org/10.1016/j.tecto.2017.08.031

Zhao, B., 1992. The Basement Properties of the Junggar Basin. *Xinjiang Petroleum Geology*, 13(3): 95–99 (in Chinese with English Abstract)

Zhao, J. M., Chen, X. F., Liu, X., 2010. A Geoscience Transect from Emin to Hami, Xinjiang, China (Including a Map of GGT). Science Press, Beijing (in Chinese)

Zhao, J. M., Cheng, H. G., Pei, S. P., et al., 2008a. Deep Structure at Northern margin of Tarim Basin. *Chinese Science Bulletin*, 53: 1544–1554 (in Chinese)

Zhao, J. M., Ma, Z. J., Yao, C. L., et al., 2008b. Analysis on Gravity-Magnetic Anomalies in Basement Geotectonic Divisions in Junggar Basin. *Xinjiang Petroleum Geology*, 29(1): 7–11 (in Chinese with English Abstract)

Zhao, J. M., Jin, Z. J., Mooney, W. D., et al., 2013. Crustal Structure of the Central Qaidam Basin Imaged by Seismic Wide-Angle Reflection/Refraction Profiling. *Tectonophysics*, 584: 174–190. https://doi.org/10.1016/j.tecto.2012.09.005

Zhao, J. M., Liu, G. D., Lu, Z. X., et al., 2003. Lithospheric Structure and Dynamic Processes of the Tianshan Orogenic Belt and the Junggar Basin. *Tectonophysics*, 376(3–4): 199–239. https://doi.org/10.1016/j.tecto.2003.07.001

Zhao, J. M., Mooney, W. D., Zhang, X. K., et al., 2006. Crustal Structure across the Altyn Tagh Range at the Northern Margin of the Tibetan Plateau and Tectonic Implications. *Earth Planetary Science Letters*, 241(3–4): 804–814. https://doi.org/10.1016/j.epsl.2005.11.003

Zhao, J. M., Shah, S. T. H., Zhang, H., et al., 2017. Density and Magnetic Intensity of the Crust and Uppermost Mantle across the Northern Margin of the Tibetan Plateau. *Physics of the Earth & Planetary Interiors*, 265: 15–22. https://doi.org/10.1016/j.pepi.2017.02.003

Zheng, J. P., Wang, F. Z., Cheng, Z. M., et al., 2000. Nature and Evolution of Amalgamated Basement of Junggar Basin Northwestern China: Sr-Nd Isotope Evidences of Basement Igneous Rock. *Earth Science*, 25(2): 179–185 (in Chinese with English Abstract)

Zheng, J. P., Sun, M., Zhao, G. C., et al., 2007. Elemental and Sr-Nd-Pb Isotopic Geochemistry of Late Paleozoic Volcanic Rocks beneath the Junggar Basin, NW China: Implications for the Formation and Evolution of the Basin Basement. *Journal of Asian Earth Science*, 29(5–6): 778–794. https://doi.org/10.1016/j.jseaes.2006.05.004